




# Comparison of the electrical conductivity of bulk and film $\text{Ce}_{1-x}\text{Zr}_x\text{O}_{2-\delta}$ in oxygen-depleted atmospheres at high temperatures

Iurii Kogut<sup>1,\*</sup> , Carsten Steiner<sup>2</sup>, Hendrik Wulfmeier<sup>1</sup>, Alexander Wollbrink<sup>1</sup>, Gunter Hagen<sup>2</sup>, Ralf Moos<sup>2</sup>, and Holger Fritze<sup>1</sup>

<sup>1</sup>Institute of Energy Research and Physical Technologies, Clausthal University of Technology, 38640 Goslar, Germany

<sup>2</sup>Department of Functional Materials, Bayreuth Engine Research Center (BERC), University of Bayreuth, 95440 Bayreuth, Germany

Received: 17 May 2021

Accepted: 14 July 2021

Published online:

17 August 2021

© The Author(s) 2021

## ABSTRACT

Featuring high levels of achievable oxygen non-stoichiometry  $\delta$ ,  $\text{Ce}_{1-x}\text{Zr}_x\text{O}_{2-\delta}$  solid solutions (CZO) are crucial for application as oxygen storage materials in, for example, automotive three-way catalytic converters (TWC). The use of CZO in form of films combined with simple manufacturing methods is beneficial in view of device miniaturization and reducing of TWC manufacturing costs. In this study, a comparative microstructural and electrochemical characterization of film and conventional bulk CZO is performed using X-ray diffractometry, scanning electron microscopy, and impedance spectroscopy. The films were composed of grains with dimensions of 100 nm or less, and the bulk samples had about 1  $\mu\text{m}$  large grains. The electrical behavior of nanostructured films and coarse-grained bulk CZO ( $x > 0$ ) was qualitatively similar at high temperatures and under reducing atmospheres. This is explained by dominating effect of Zr addition, which masks microstructural effects on electrical conductivity, enhances the reducibility, and favors strongly electronic conductivity of CZO at temperatures even 200 K lower than those for pure ceria. The nanostructured  $\text{CeO}_2$  films had much higher electrical conductivity with different trends in dependence on temperature and reducing atmospheres than their bulk counterparts. For the latter, the conductivity was dominantly electronic, and microstructural effects were significant at  $T < 700$  °C. Nanostructural peculiarities of  $\text{CeO}_2$  films are assumed to induce their more pronounced ionic conduction at medium oxygen partial pressures and relatively low temperatures. The defect interactions in bulk and film CZO under reducing conditions are discussed in the framework of conventional defect models for ceria.

Handling Editor: Till Froemling.

Address correspondence to E-mail: iurii.kogut@tu-clausthal.de

## Introduction

Ceria/zirconia mixed oxides  $\text{Ce}_{1-x}\text{Zr}_x\text{O}_{2-\delta}$  (CZO) are crucial components of state-of-the-art technologies to minimize hazardous emissions of combustion engines in the environment. The most known devices to rely on CZO are the three-way catalytic converters (TWC) used for after treatment of the exhausts of most gasoline-powered vehicles [1–6]. The interest in CZO is motivated by its outstanding catalytic properties due to its much lower reduction enthalpies and higher levels of attainable oxygen non-stoichiometry  $\delta$  and, hence, its superior oxygen storage or release capacity, in contrast to pure  $\text{CeO}_{2-\delta}$  [4–16]. The development of oxygen non-stoichiometries (facilitated by high temperatures and decreasing oxygen partial pressure,  $p\text{O}_2$ ) in ceria-based compounds is caused by the loss of oxygen and related formation of positively charged oxygen vacancies that are compensated by conduction electrons (reduced Ce). They enhance the electrical conductivity  $\sigma$  [14–17], which, thus, becomes an indirect measure of the reduction degree. In nominally undoped CZO, the favorable effect on the conductivity is assigned to the substitution of Zr for Ce. It exerts strain on the crystal lattice, thus, favoring an extensive formation of oxygen vacancies, which is associated with structural relaxation through reduction of  $\text{Ce}^{4+}$  to  $\text{Ce}^{3+}$  ions. This boosts the electronic transport at considerably higher  $p\text{O}_2$  and lower reduction temperatures than for pure  $\text{CeO}_{2-\delta}$  [4, 7, 10–13]. Despite the obvious influence of Zr addition, the reduction kinetics also depends upon structural peculiarities of the catalyst materials, e.g., on extended surfaces and on grain boundaries (GB) in thin films or nanostructured bulk ceramics [4, 7, 10, 18–26]. In these low-dimensional CZO morphologies, even a further decrease in the reduction enthalpy and a strong increase in the electrical conductivity over that of bulk materials with coarse grains can be expected [24–28]. This implies larger non-stoichiometries for a given set of temperatures and  $p\text{O}_2$ . From an application point of view, understanding the relations between microstructure and reducibility combined with utilization of simple fabrication methods would allow for the development of  $\text{Ce}_{1-x}\text{Zr}_x\text{O}_{2-\delta}$  films with superior catalytic properties, paving the way toward less costly high-performance miniaturized TWCs.

Previously, we reported on the high-temperature electrical conductivity ( $\sigma$ ) and non-stoichiometry ( $\delta$ ) of  $\text{Ce}_{1-x}\text{Zr}_x\text{O}_{2-\delta}$  films in oxygen-deficient atmosphere [29], where DC measurements and impedance spectroscopy were applied for determining  $\delta$ , in conjunction with a resonant nanobalance method. A correlation between the conductivity  $\sigma$  and non-stoichiometry  $\delta$  of CZO films in terms of slopes derived from log–log representations of their  $p\text{O}_2$ -dependences at 800–900 °C was evident. However, at lower temperatures (600–700 °C), the conductivity of CZO films, especially of pure  $\text{CeO}_{2-\delta}$ , barely correlated with the non-stoichiometry parameter  $\delta$ . The question arose, whether the observed phenomena were specific to the fact that studied  $\text{Ce}_{1-x}\text{Zr}_x\text{O}_{2-\delta}$  were films. To address this question, the present study aims to compare the electrical conductivities of bulk ceramics and films of  $\text{Ce}_{1-x}\text{Zr}_x\text{O}_{2-\delta}$  with  $0 \leq x \leq 0.67$ , basing on the fundamental prerequisite that they were prepared from the same starting materials to exclude different impurity levels. This should enable us to figure out whether possible differences

- (1) are specifically related to the dimensions and microstructures of films or
- (2) whether the electrochemical behavior of bulk and film  $\text{Ce}_{1-x}\text{Zr}_x\text{O}_{2-\delta}$  could be equally described in the framework of conventional bulk defect chemical models for ceria derivatives.

The starting point is the microstructural characterization of both types of CZO samples. Subsequently, their electrical properties are measured and analyzed by impedance spectroscopy in two- and four-electrode configurations.

## Materials and methods

Bulk ceramic specimens of  $\text{CeO}_2$ – $\text{ZrO}_2$  solid solutions ( $\text{Ce}_{1-x}\text{Zr}_x\text{O}_{2-\delta}$ ; CZO;  $0 \leq x \leq 0.67$ ) were fabricated by solid-state reactions with calcination and sintering at 1650 °C as in details reported in our previous work [29]. The resulting pellets served as targets for pulsed laser deposition (PLD) of CZO films onto sapphire substrates ( $\text{Al}_2\text{O}_3$ ) using a 248 nm excimer KrF laser (COMPex, Coherent, Inc., Santa Clara, USA) operated at pulse rate of 10 Hz with 200 mJ pulse energy. The depositions were conducted in an evacuated chamber ( $5 \times 10^{-4}$ – $10^{-3}$  Pa during sputtering) with no

intentional heating of the substrates. After deposition, the films were heat-treated in air at 900 °C for 1 h in order to restore the oxygen stoichiometry [29].

The  $\text{Ce}_{1-x}\text{Zr}_x\text{O}_{2-\delta}$  pellets and films were characterized by X-ray diffraction (XRD) in parallel beam ( $2\theta-\omega$ ) geometry enabled by Göbel mirror within  $2\theta = (25-100)^\circ$  with  $0.02^\circ$  resolution and 1300 s integration time per step using the Bruker D8 ADVANCE X-ray diffractometer (Bruker AXS GmbH, Karlsruhe, Germany) with a  $\text{Cu-K}\alpha_1 + \text{Cu-K}\alpha_2$  radiation ( $\lambda = 1.5419 \text{ \AA}$ ). The pre-calibrated instrumental line broadening profile of the diffractometer was available from the device manufacturer, which enabled estimation of crystallites sizes by Scherrer's equation [30]. A whole pattern fitting combined with a Rietveld refinement (WPF) [31, 32] was implemented for further evaluation of crystallographic properties of CZO. The microstructural and elemental analysis of  $\text{Ce}_{1-x}\text{Zr}_x\text{O}_{2-\delta}$  was performed with scanning electron microscope and energy-dispersive X-ray spectroscopy (SEM/EDS, CamScan 44, CamScan Electron Optics Ltd., Waterbeach, UK) and, additionally, with a high-resolution SEM (Omicron NanoSAM, Scienta Omicron AB, Uppsala, Sweden). With a confidence level of 95.4%, the uncertainties of the determined elemental fractions were about 1.5% for Ce and Zr and 3.2% for oxygen. The  $\text{Ce}_{1-x}\text{Zr}_x\text{O}_{2-\delta}$  bulk samples and PLD targets also contained non-intentional impurities of several 100 ppm [29], which may cause the formation of extrinsic oxygen vacancies (see sec. 3.3).

For electrical conductivity measurements, the bulk 1.5–2-mm-thick CZO pellets were cut into about 8 mm-long and 2.1–3.5 mm-wide bars. The PLD  $\text{Ce}_{1-x}\text{Zr}_x\text{O}_{2-\delta}$  films had a size of  $8 \times 8 \text{ mm}^2$  and thicknesses of about  $2 \mu\text{m}$  ( $x = 0, 0.2$  and  $0.33$ ) and  $4-5 \mu\text{m}$  ( $x = 0.5, 0.67$ ). The electrical conductivity of bulk and film CZO was analyzed in the four- (IS4) and two-contact (IS2) configuration, respectively, by impedance spectroscopy (IS) using the Solartron 1260 impedance gain-phase analyzer assisted by the high-impedance measuring bridge Solartron 1296 (Solartron Analytical, Leicester, UK). Two ring Pt electrodes were bound at the edges of the bulk bars (current leads) and another two ring electrodes—at 4–6 mm from each other in the middle of the bars (voltage leads). For films, two stripe electrodes were applied 2–4 mm away from each other by screen printing of a Pt paste and firing at 900 °C for 1 h in air. The uncertainties of geometric parameters for

bulk and film samples are typically 1.5%, and the accuracy of average thicknesses of films is within error margins of 3.2–11.3%. The studied specimens are depicted in Fig. 1. The IS4 data were taken in a frequency range of  $1-10^7 \text{ Hz}$  with a rms AC voltage amplitude of 20 mV and the IS2—in the range of  $10-10^6 \text{ Hz}$  and a rms AC voltage of 50 mV. From the differences in both spectra, one may identify electrode effects [33] and exclude them from further interpretation of true electrical conductivity of CZO.

Additionally, the DC electrical conductivity of bulk and film CZO was determined in two-contact configuration (also applied for IS2 of bulks) by a Keithley DVM 2700 digital multimeter (Keithley Instruments, Solon, OH, USA). The conductivity was measured under isothermal conditions at 600, 700, 800, and 900 °C in a gastight furnace with a temperature control enabled by the Type S thermocouple located in the vicinity to the measured samples and by a Pt100 thermoresistor compensating the temperature drifts at the cold end of the thermocouple. To establish reducing atmosphere in the chamber, i.e., oxygen partial pressures  $p\text{O}_2$  between  $10^{-26}$  and 0.2 bar, the oxygen ion pump technique was applied [34]. Small  $\text{O}_2$  amounts were admixed to the flow (20 mL/min) of a reducing gas mixture (99.5% Ar–0.5%  $\text{H}_2$ ). The uncertainty of evaluated electrical conductivities was in the range of 2–4% for bulk and 3–6% for film specimens. Since the sample dimensions do not contribute in the determination of slopes in  $\sigma(T)$  and  $\sigma(p\text{O}_2)$  dependences of electrical conductivity, the uncertainties of these coefficients were lower and amounted to about 3%.

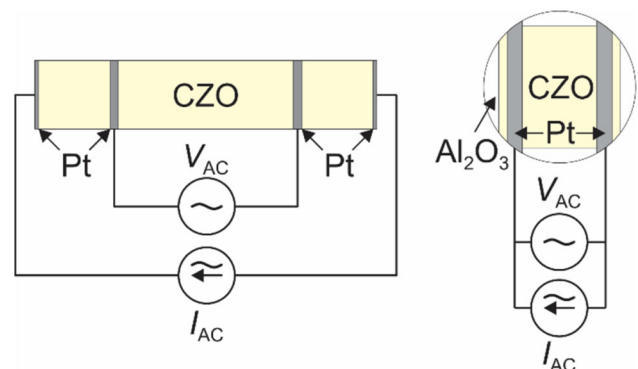


**Figure 1** Schematic representation of bulk (left) and film (right)  $\text{Ce}_{1-x}\text{Zr}_x\text{O}_{2-\delta}$  samples and corresponding contact configurations for IS and DC measurements of their electrical conductivity.

## Results and discussion

In order to elucidate the possible differences in the temperature- and  $pO_2$ -dependent behavior of film and bulk ceria/zirconia mixed oxides, first a comparative study of their microstructural peculiarities is performed. Then, the analysis of temperature dependences of their electrical conductivity in air and in reducing atmosphere using the impedance spectroscopy in 2- and 4-electrode configurations is conducted.

### Microstructural and chemical characterization of $Ce_{1-x}Zr_xO_{2-\delta}$

The starting point is the microstructural characterization of CZO by XRD and SEM/EDS. In Fig. 2, typical XRD patterns for bulk samples and PLD films are compared. Table 1 provides the relevant characteristics of  $Ce_{1-x}Zr_xO_{2-\delta}$ , extracted by the WPF. The ceria-rich compounds ( $x = 0, 0.2$  and  $0.33$ ) crystallized in face-centered cubic phase of the  $CaF_2$ -type ( $Fm\bar{3}m$ ) [35], and ZrO<sub>2</sub>-rich materials ( $x = 0.5, 0.67$ ) crystallized in metastable tetragonal  $P42/nmc$  phase [36]. The CZO films were found to fairly reproduce the crystalline structure of their bulk counterparts. However, we note a preferred orientation of the cubic CZO on sapphire, which is evidenced by the suppression of reflections that correspond to planes parallel to or inclined toward the  $a$ -axis (e.g., the (200) and (311) reflections in Fig. 2). Similar results for

CeO<sub>2</sub>-based layers on Al<sub>2</sub>O<sub>3</sub> substrates were reported in [23, 37].

The determined lattice parameters are consistent with those reported in the literature [7, 23, 35, 36] and, as expected, decrease linearly with increasing Zr content in cubic samples (Fig. 3, Table 1). The average grain sizes  $r_c$ , both in bulk and film samples, show a trend to decrease with increasing Zr content (Table 1), but in PLD layers on sapphire, the grains were markedly smaller by a factor of about 20 (up to 40 in case of  $Ce_{0.8}Zr_{0.2}O_{2-\delta}$ ). The above trend is at least for  $x = 0$  and  $0.2$  consistent with the literature [19].

The chemical compositions of PLD and bulk CZO are also similar (Table 2). The PLD layers on sapphire are composed of large flat and homogeneous planar “islands” with lateral dimensions exceeding several tens of micrometers (Fig. 4b, d). A closer look into the interior of large planar features (inset in Fig. 4b) showed an array of regularly dispersed and densely packed grains with dimensions less than 200 nm. This agrees well with the grain size as determined by XRD. We note also the irregularly shaped relatively large particles randomly dispersed over the surface of films, whose surface density increased with ZrO<sub>2</sub> fraction in the material, as previously reported in [29]. Within the measurement error, the EDS analysis of the particles revealed the same composition as the “islands”.

In contrast to film samples, the microstructure of bulk specimens is characterized by several

**Figure 2** Typical XRD profiles of  $Ce_{1-x}Zr_xO_{2-\delta}$ , showing a nearly perfect match with the reference patterns for nominal cubic ( $Fm\bar{3}m$ ) CeO<sub>2</sub> and tetragonal ( $P42/nmc$ )  $Ce_{0.5}Zr_{0.5}O_2$ . The reflections of platinum originate from the electrodes deposited on the films.

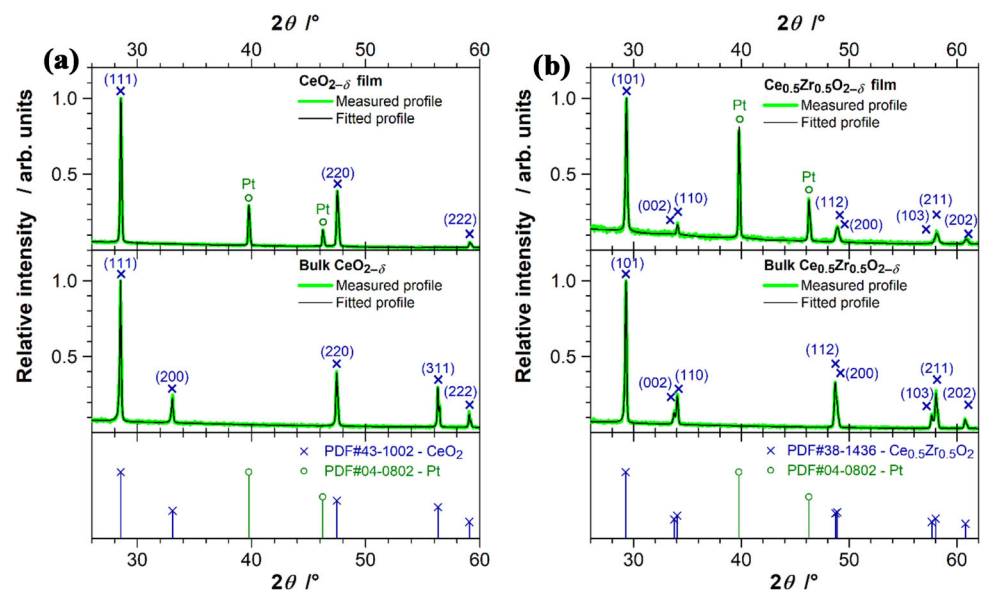




**Table 1** Lattice parameters and average grain dimensions ( $r_c$ ) of bulk and film  $Ce_{1-x}Zr_xO_{2-\delta}$

Sample composition	Bulk samples			Film samples						
	Lattice parameters in Å			$r_c$ in nm	$R_p^a$ in %	Lattice parameters in Å				
	$a$	$b$	$c$			$a$	$b$	$c$		
CeO <sub>2</sub>	5.4119(5)			1102	8.4	5.4121(26)			54	4.9
Ce <sub>0.8</sub> Zr <sub>0.2</sub> O <sub>2</sub>	5.3520(12)			924	9.5	5.3536(21)			29	6.6
Ce <sub>0.67</sub> Zr <sub>0.33</sub> O <sub>2</sub>	5.3184(11)			888	10.3	5.3209(86)			48	7.2
Ce <sub>0.5</sub> Zr <sub>0.5</sub> O <sub>2</sub>	3.7165(3)	5.3065(4)		792	9.7	3.7208(23)	5.3005(48)		43	6.8
Ce <sub>0.33</sub> Zr <sub>0.67</sub> O <sub>2</sub> <sup>b</sup>	3.6765(5)	5.2715(9)		836	9.1	3.6796(42)	5.2676(104)		37	12.1

The numbers in brackets denote the uncertainties in the last digits of lattice parameters

<sup>a</sup> $R_p$  stands for the residual fit error

<sup>b</sup>The parameters provided only for stable  $t$ -phase, though also the metastable  $t'$  phase was observed [29, 35]

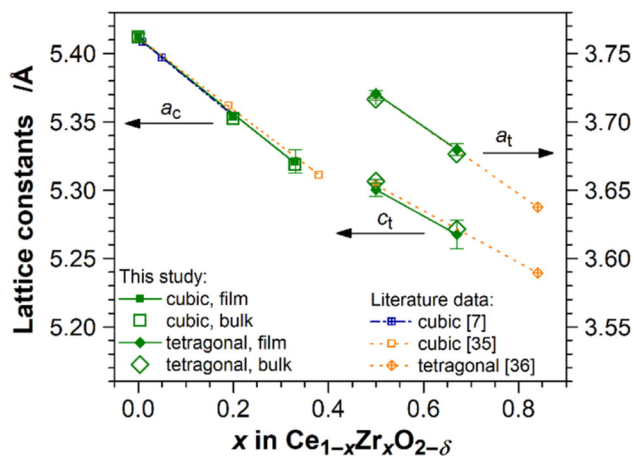


**Figure 3** Variation of lattice constants  $a_c$  for cubic and  $a_t$  and  $c_t$  for tetragonal CZO samples with Zr fraction.

micrometer large particles composed of fused, about 1  $\mu$ m large grains (see, e.g., Fig. 4c), and porosity,<sup>1</sup> especially evident in Zr-containing CZO (Fig. 4a, c).

<sup>1</sup> The density of as-sintered bulk samples (measured by weighing method and gas pycnometer micromeritics® Accy-Pyc 1330, Norcross, USA) was not lower than about 90% of theoretical density. The estimation of effective conductive volume of the samples results in conductivity correction of less than 27%. As in this study, a rather qualitative comparison of film and bulk CZO is intended, the reported conductivities are not corrected for porosity.

### Temperature dependence of electrical conductivity of CZO

We applied impedance spectroscopy to find out whether these microstructural features affect the electrical behavior of CZO and which phenomena are responsible for their conductivity behavior at typical operation temperatures of TWCs. Previously, the conductivity of CZO films was measured in lateral direction using the IS2 approach [29]. In this configuration, the complex impedance spectra of coarse-grained ceria typically contain well-separated frequency dispersions (semicircles) corresponding to grain interior (high-frequency domain) and grain boundary (GB; low frequency) resistances [12, 23, 24, 28, 37, 39–41]. As the temperature increases (or  $pO_2$  decreases), the high-frequency contributions become less distinguishable due to the exponential increase of the characteristic frequency for bulk transport with temperature [41]. Eventually, with a diminishing low-frequency part, and sometimes covered by stray capacitances, both contributions become indistinguishable essentially turning into a condensed point at the intersection with real impedance axis [28, 41]. At high temperatures, the conductivity is, thus, treated as a total conductivity [23, 28, 37, 41]. In nominally undoped ceria, it was found to be dominantly electronic [12, 24, 27, 28, 42]. In case of nanostructured materials, with decreasing grain dimensions, the GB contributions may overlap with that of the grain interiors, making it hard to distinguish them [26, 41, 43]. Furthermore, in case of films, the presence of large stray capacitances (since

**Table 2** Chemical composition of bulk and PLD film  $\text{Ce}_{1-x}\text{Zr}_x\text{O}_{2-\delta}$ , evaluated by EDS

Nominal composition	Bulk samples				Film samples			
	Measured content in at.-%			Actual composition	Measured content in at.-%			Actual composition
	Ce	Zr	O		Ce	Zr	O	
$\text{CeO}_2$	34.3	–	65.7	$\text{CeO}_{1.92}$	34.4	0	65.6	$\text{CeO}_{1.91}$
$\text{Ce}_{0.8}\text{Zr}_{0.2}\text{O}_2$	n/a	n/a	n/a	n/a	27.2	6.9	65.9	$\text{Ce}_{0.8}\text{Zr}_{0.2}\text{O}_{1.94}$
$\text{Ce}_{0.67}\text{Zr}_{0.33}\text{O}_2$	23.8	11.0	65.2	$\text{Ce}_{0.68}\text{Zr}_{0.32}\text{O}_{1.87}$	23.1	11.2	65.7	$\text{Ce}_{0.67}\text{Zr}_{0.33}\text{O}_{1.91}$
$\text{Ce}_{0.5}\text{Zr}_{0.5}\text{O}_2$	19.4	15.2	65.4	$\text{Ce}_{0.56}\text{Zr}_{0.44}\text{O}_{1.89}$	17.6	17.0	65.4	$\text{Ce}_{0.51}\text{Zr}_{0.49}\text{O}_{1.89}$
$\text{Ce}_{0.33}\text{Zr}_{0.67}\text{O}_2$	12.2	21.2	66.6	$\text{Ce}_{0.37}\text{Zr}_{0.63}\text{O}_{1.99}$	11.5	21.4	67.1	$\text{Ce}_{0.35}\text{Zr}_{0.65}\text{O}_{2.04}$

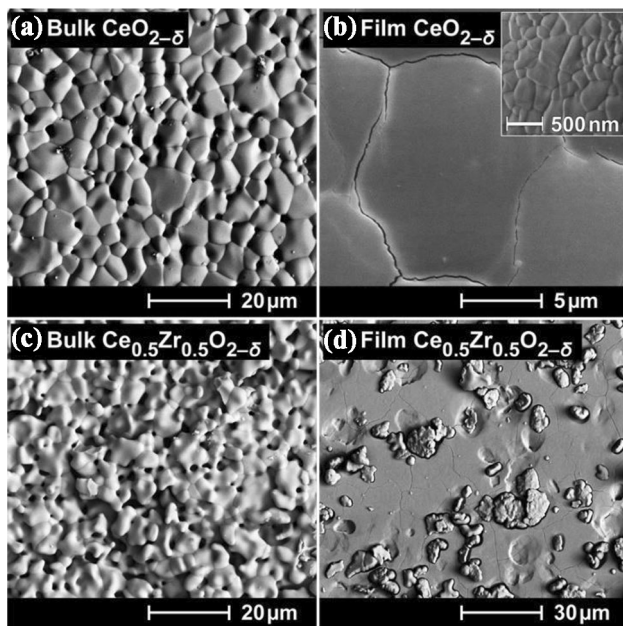


**Figure 4** SEM images of bulk (a, c) and PLD film (b, d)  $\text{Ce}_{1-x}\text{Zr}_x\text{O}_{2-\delta}$ . The inset in (b) shows high-resolution SEM of  $\text{CeO}_{2-\delta}$  “island” microstructure. Images (a, c and d) are acquired in back-scattered electron contrast mode, showing a single-phase nature of the samples. The cracks observed in  $\text{CeO}_{2-\delta}$  films are expected to close at increased temperatures due to combined action of thermal and chemical expansion, inherent for ceria [29]. A thermal expansion mismatch between film and substrate  $\Delta\alpha$  is estimated to be  $\approx 5$  ppm/K [29]. With chemical expansion coefficient of 0.1 for ceria ([38]), for the temperature increase by 600 K and non-stoichiometry of 0.01, the total expansion of an “island” is about 0.4%.

the volume between electrodes is small) may mask the GB-related contribution [23, 27, 28, 37]. Hence, in this work, we combined the IS4 and IS2

configurations for bulk samples to include the conditions of PLD films characterization of our previous work [29].

In Fig. 5, typical complex resistivity  $\rho''(\rho')$  spectra for bulk and film  $\text{Ce}_{1-x}\text{Zr}_x\text{O}_{2-\delta}$  at moderate temperatures and oxidizing conditions are presented (with  $\rho'$  and  $\rho''$  being the real and imaginary components of complex resistivity, respectively). For bulk CZO materials, two semicircles on the  $\rho''(\rho')$  plots are obtained with an IS2 approach, whereas only one semicircle is resolved with IS4 (Fig. 5a, inset of Fig. 5b). The high-frequency part (first semicircle from 0 to about  $550 \Omega\text{m}$  in Fig. 5a) of IS2 and the single semicircle from IS4 overlap, suggesting the same localization and mechanism of this charge transfer contribution in the samples. We attribute it to the grain interior conductivity (index G)  $\sigma_G$  of polycrystalline CZO with the resistance  $R_G$  and a capacitance expressed by the constant phase element  $CPE_G$  accounting for the non-ideal capacitive behavior of the material. The similarity of capacitances on the order of  $10^{-12}$  F, as seen by the least-square fitting (LS) of the parameters of  $R_G|CPE_G$  (see EEC in Fig. 5a) to IS2 and IS4 spectra, supports this assumption. The  $R_W$  in the depicted EEC stands for the resistance of cables and electrical connections in the equipment. Obviously, the low-frequency semicircle observed in IS2 is eliminated by the IS4 approach. Hence, the charge transfer in this frequency domain contribution can be attributed to the polarization effects at the interface between the CZO and Pt-electrodes [33, 39, 41, 44–47]. Since the polarization effect is related to a specific measurement approach, it will not be further evaluated and

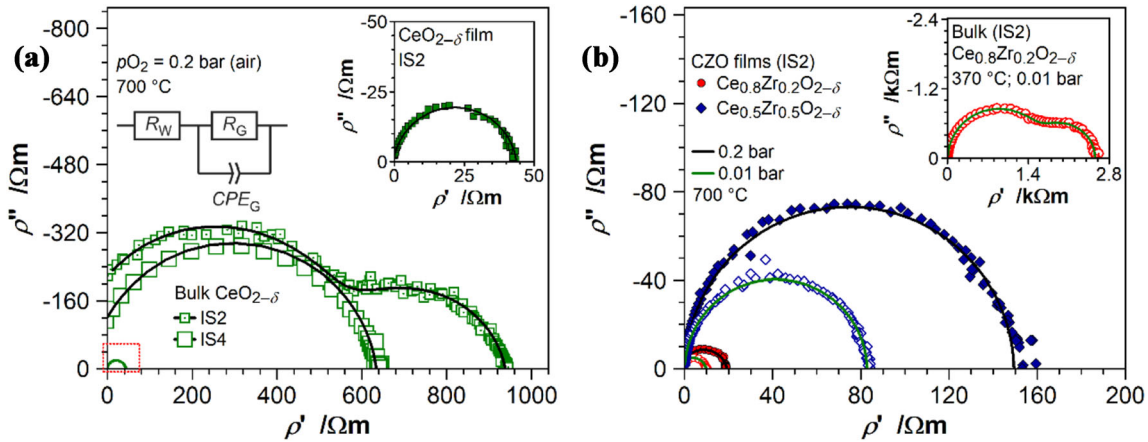


**Figure 5** Complex resistivity  $\rho''(\rho')$  spectra for bulk and film  $\text{CeO}_{2-\delta}$  in air (a) and for  $\text{Ce}_{1-x}\text{Zr}_x\text{O}_{2-\delta}$  at different oxygen partial pressures (b). Solid lines represent the LS-fit of IS to equivalent electrical circuit (EEC) pictured in (a). The insets in (a) show the

equivalent circuit without the electrode contribution that includes  $R_W$  and  $R_G|CPE_G$  (see text, left) and the enlarged IS spectra for curves boxed in a red frame (right).

discussed. The film CZO specimens showed only one semicircle in IS2 and, apparently, no polarization-related contribution.<sup>2</sup> Similar results were obtained for impedance spectra of ceria-based thin films deposited with PLD onto sapphire substrates by other research groups [23, 27, 37].

Distinguishing between the conductivity via grain interior (G) and via grain boundary (GB) is practically impossible when only one semicircle can be evaluated. Insights based on the dielectric constant of the film are not feasible, as it cannot be calculated due to the dominating stray capacitance for lateral IS measurements. Hence, in further, we analyze only the total resistance  $R_{\text{tot}} = R_G + R_{\text{GB}}$  of films. It is equivalent to our measured DC resistance.

The temperature dependences of  $\sigma_{\text{tot}}$  for films and bulk materials in air are shown in Fig. 6a. Despite the discrepancies in the absolute values of conductivities (likely, due to uncertainty of sample dimensions and porosity of bulk samples, see sec. 2) for  $\text{Ce}_{1-x}\text{Zr}_x\text{O}_{2-\delta}$  with  $x$  of 0.2–0.5, the slopes in their Arrhenius representations are identical within the error margins. For  $\text{Ce}_{0.8}\text{Zr}_{0.2}\text{O}_{2-\delta}$ , the conductivities match. Together with linear  $\log(\sigma)$  vs.  $1/T$  dependences and very similar activation energies  $E_a$  for bulk and film CZO (Table 3), this observation implies that same conductance mechanism occurs in both kinds of materials between 600 and 900 °C. Moreover, the  $E_a$  values

are consistent with literature data for bulk- and nano- $\text{Ce}_{1-x}\text{Zr}_x\text{O}_{2-\delta}$  [11, 12, 18, 23, 27, 48]. Based on the similarities observed for bulk and film  $\text{Ce}_{1-x}\text{Zr}_x\text{O}_{2-\delta}$  ( $0.2 \leq x \leq 0.5$ ), we conclude that the conductivity of  $\text{CeO}_2\text{-ZrO}_2$  films is dominated by grain interior charge transport.

Essential observation is that for bulk  $\text{Ce}_{1-x}\text{Zr}_x\text{O}_{2-\delta}$  with  $x \geq 0.2$ , the grain conductivity component  $\sigma_G$  constitutes the total conductivity  $\sigma_{\text{tot}}$  of the specimens at temperatures above 500 °C (Fig. 6b), becoming a sole conductivity-limiting (i.e., dominant) factor in the concerned temperature range of 600–900 °C. In  $\text{CeO}_{2-\delta}$ ,  $\sigma_G$  becomes dominant only at  $T > 680$  °C (Fig. 6b). The observed transition is accompanied by a change in the slope of the  $\log(\sigma_G)-1/T$  representation, i.e., the conductivity mechanism changes, which is indicated by a steep increase of  $E_a$  (Table 3). We have found that in Zr-containing bulk CZO the change in the slope occurred when the electrode component (second semicircle in IS2, e.g., seen only at  $T < 500$  °C in the inset of Fig. 5b) was no longer resolved, eventually turning the spectra into a condensed point at the intersection with the  $\rho'$ -axis. For bulk  $\text{CeO}_{2-\delta}$ , these IS features occurred only at  $T > 700$  °C or at lower  $p\text{O}_2$ . According to the literature, such behavior can be ascribed to the transition from dominant ionic to dominant electronic bulk conductivity with increasing temperature [28, 41–43]. The evaluated high-temperature  $E_a$  values of about 2 eV for bulk  $\text{CeO}_{2-\delta}$  and 1.5–1.6 eV for Zr-containing CZO are consistent with those reported for dominant intrinsic electronic conduction of  $\text{CeO}_2$  and

<sup>2</sup> For bulk samples, the ratio of length to cross-sectional area is about  $1 \text{ mm}^{-1}$ , whereas in films, it is  $100\text{--}250 \text{ mm}^{-1}$ . Consequently, the films exhibit much higher resistances, and the interface polarization becomes negligible.

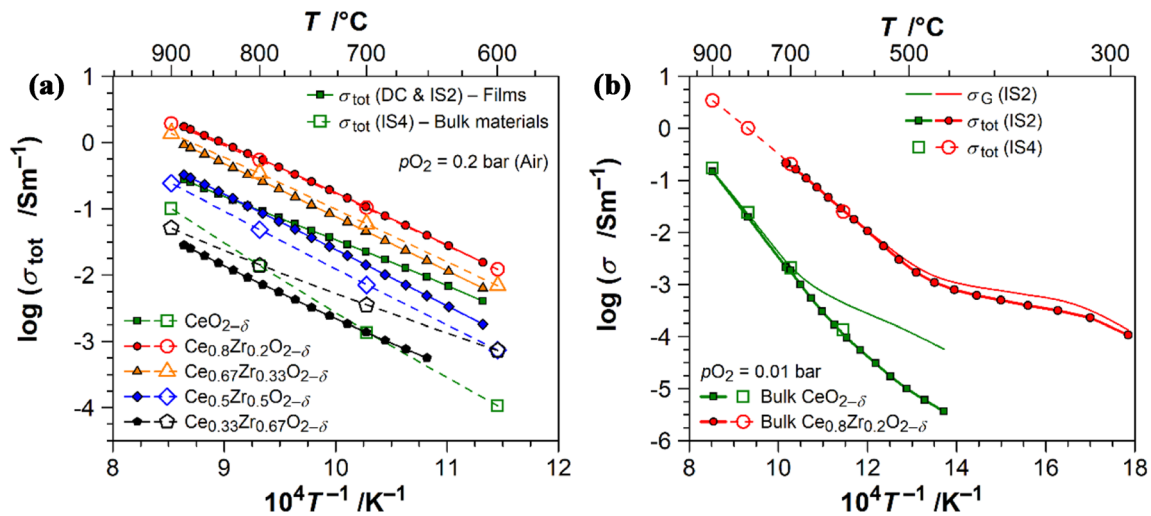


**Figure 6** Temperature dependences of electrical conductivities of  $\text{Ce}_{1-x}\text{Zr}_x\text{O}_{2-\delta}$  in air (a) and of the grain interior ( $\sigma_G$ ) contribution in total electrical conductivity  $\sigma_{\text{tot}}$  of bulk CZO (b).

**Table 3** Activation energies  $E_a$  (in eV) of conductivities for film and bulk  $\text{Ce}_{1-x}\text{Zr}_x\text{O}_{2-\delta}$  as derived from IS2 and IS4 complex impedance measurements

Nominal composition	Total conductivity $\sigma_{\text{tot}}$ 600–900 °C		Grain interior conductivity $\sigma_G$ (bulk CZO; IS2)	
	Film (IS2)	Bulk (IS4)	Moderate temperatures	High temperatures
$\text{CeO}_2$	$1.33 \pm 0.15$	$2.02 \pm 0.14$	$0.78 \pm 0.1$ (450–650 °C)	$2.09 \pm 0.16$ (700–900 °C)
$\text{Ce}_{0.8}\text{Zr}_{0.2}\text{O}_2$	$1.50 \pm 0.11$	$1.50 \pm 0.09$	$0.27 \pm 0.04$ (350–450 °C)	$1.43 \pm 0.14$ (500–700 °C)
$\text{Ce}_{0.67}\text{Zr}_{0.33}\text{O}_2$	$1.60 \pm 0.13$	$1.56 \pm 0.12$		
$\text{Ce}_{0.5}\text{Zr}_{0.5}\text{O}_2$	$1.66 \pm 0.16$	$1.70 \pm 0.14$		
$\text{Ce}_{0.33}\text{Zr}_{0.67}\text{O}_2$	$1.56 \pm 0.19$	$1.25 \pm 0.08$		

CZO at elevated temperatures in literature [11, 12, 24, 27, 42, 48]. Noteworthy, the conductivity activation energy includes the reduction enthalpy  $H_r$  and migration enthalpy  $H_m$  ( $E_a = H_r/3 + H_m$ ), where  $H_m = 0.35\text{--}0.4$  eV describes the small polaron hopping mechanism [11]. Thereof resulting  $H_r$  values of about 4.8 and 3.1 eV are consistent with expected reduction enthalpies for  $\text{CeO}_{2-\delta}$  and  $\text{Ce}_{1-x}\text{Zr}_x\text{O}_{2-\delta}$ , respectively [11, 42]. At low temperatures (before the transition), the  $E_a$  values are much lower (Table 3). As the reduction degree at low temperatures in air is negligible [14], we suggest that in these conditions the ionic conductivity via intrinsic Frenkel defects (intrinsic oxygen vacancies formed according to  $\text{CeO}_2 = \text{Ce}_{\text{Ce}}^{\times} + 2\text{V}_{\text{O}}^{\bullet\bullet} + 2\text{O}_i^{\prime\prime}$ ) and/or extrinsic oxygen vacancies introduced by acceptor (A) impurities ( $\text{A}_2\text{O}_3 = 2\text{A}'_{\text{Ce}} + \text{V}_{\text{O}}^{\bullet\bullet} + 3\text{O}_i^{\prime\prime}$ ) dominates. In the latter case, the electroneutrality of the system requires compensation by electron holes (concentration fixed by impurity). They contribute to the electrical

conductivity at temperatures below 750 °C [12]. Our  $E_a$  value of 0.78 eV for  $\text{CeO}_{2-\delta}$  is close to 0.86 eV reported in [12] for the same temperature range. As earlier reported in [29], our ceria/zirconia solid solutions were overall less pure than  $\text{CeO}_{2-\delta}$ , which may explain the lower  $E_a$  for conductivity of  $\text{Ce}_{1-x}\text{Zr}_x\text{O}_{2-\delta}$  at low temperatures. In summary, we suggest that the changes in the apparent activation energies of conductivity depicted in Fig. 6b and Table 3 describe the transition from thermally activated extrinsic impurity-controlled (mixed) charge transport at low temperatures to intrinsic reduction-controlled transport at high temperatures. In the latter regime, the concentrations equation  $[\text{Ce}'_{\text{Ce}}] = 2[\text{V}_{\text{O}}^{\bullet\bullet}] = 2\delta$  applies, and, due to much higher mobility of electrons, the conductivity is dominantly electronic.

As stated earlier, the conductivity behavior of film and bulk  $\text{Ce}_{1-x}\text{Zr}_x\text{O}_{2-\delta}$  was qualitatively similar. Meanwhile, pure ceria films show almost two orders



of magnitude higher electrical conductivity and much lower  $E_a$  in contrast to bulk samples. According to the literature, this is an expected behavior explained by the impact of the higher GB density in nanostructured materials, which facilitates the charge transfer and decreases the apparent activation energy of  $\sigma_{\text{tot}}$  [23, 24, 26, 27, 43].

All in all, the insights from the temperature dependences of  $\sigma_G$  of CeO<sub>2</sub> and CZO with respect to practical application point on the obvious beneficial effect of substituting Zr for Ce. That is, the addition of Zr, essentially, greatly decreases the reduction enthalpy and leads to a strongly dominating electronic conductance of Ce<sub>1-x</sub>Zr<sub>x</sub>O<sub>2-δ</sub> at temperatures even about 200 K lower than for pure CeO<sub>2</sub>. Hence, the Ce<sub>1-x</sub>Zr<sub>x</sub>O<sub>2-δ</sub> mixed oxides are mainly electronic conductors in a much broader temperature range than pure CeO<sub>2</sub> and, compared to effect of Zr addition, the influence of their microstructural properties is marginal. Furthermore, since the dominant electronic conductivity in ceria/zirconia mixed oxides is related to the concentration of oxygen vacancies (oxygen non-stoichiometry  $\delta$ ) inside the material, these effects provide also the basis to electrically determine the actual oxygen storage level of TWC, either by direct current measurements [49] or by high-frequency methods [50], supported by the modelling conducted in [51].

### Electrical conductivity of Ce<sub>1-x</sub>Zr<sub>x</sub>O<sub>2-δ</sub> under reducing atmospheres

The analysis of the total electrical conductivity of Ce<sub>1-x</sub>Zr<sub>x</sub>O<sub>2-δ</sub> in reducing atmospheres further supports the conclusion about the crucial effect of Zr substitution for Ce in CZO materials (Fig. 7). For both kinds of samples with  $0 < x \leq 0.67$ , the trends in the  $\sigma_G$  dependences on  $p\text{O}_2$  are qualitatively similar and the negative slopes obtained in the whole studied range of  $p\text{O}_2$  and at temperatures of 700–900 °C prove the dominating electronic conduction of CeO<sub>2</sub>–ZrO<sub>2</sub>. Both film and bulk CZO with  $x \geq 0.2$  show a classic behavior that can be derived from conventional defect chemical models of ceria and its derivatives, as described, e.g., in [11, 14, 15, 18, 52]. For discussion of our data, we introduce also small acceptor (impurity) concentrations (see sec. 2).

At the highest temperature of 900 °C (Fig. 7), the variation of  $\sigma_G$  with  $(p\text{O}_2)^{-\frac{1}{6}}$  at moderate  $p\text{O}_2$  transits

to dependences with lower exponents (hereafter, designated as  $-\frac{1}{n}$ ) at decreased oxygen potentials, which reflects the transition from intrinsic conductivity regime (dominated by small polaron hopping at Ce'<sub>Ce</sub>/Ce<sup>x</sup><sub>Ce</sub> sites [14, 15]) to a conductivity dominated by strong defect interactions, assumed to lead to the formation of either dimer (Ce'<sub>Ce</sub>V<sup>••</sup><sub>O</sub>)<sup>•</sup> [18, 52] or trimer (Ce'<sub>Ce</sub>V<sup>••</sup><sub>O</sub>Ce'<sub>Ce</sub>)<sup>x</sup> [16] defect associates. In the former regime, the concentration of intrinsically generated oxygen vacancies [V<sup>••</sup><sub>O</sub>]<sub>int</sub> is much larger than that of extrinsic vacancies fixed by acceptor impurity ([V<sup>••</sup><sub>O</sub>]<sub>ext</sub>), and electronic conductivity strongly exceeds the ionic conductivity that stem from mobile oxide ion vacancies ( $\sigma_{\text{Ge}} \gg \sigma_{\text{GV}_\text{O}}$ ) [18].

At lower  $p\text{O}_2$ , the concentration of defect associates increases, leading to a  $\sigma_G \sim (p\text{O}_2)^{-\frac{1}{n}}$  dependence with  $4 \leq n < 6$  [18, 52]. Following that, with further decreasing of oxygen partial pressure, the electrical conductivity reaches a plateau/maximum, which corresponds to the condition when concentrations of reduced and non-reduced cerium ions become equal [Ce<sup>3+</sup>] = [Ce<sup>4+</sup>] and, consequently, the small polaron hopping mechanism can no longer be supported [11]. At even further decrease in oxygen potential, [Ce<sup>3+</sup>] > [Ce<sup>4+</sup>] applies, and the conductivity decreases. This behavior is clearly evidenced at highest temperatures for Ce<sub>1-x</sub>Zr<sub>x</sub>O<sub>2-δ</sub> with  $x = 0.5$  and 0.33 (Fig. 7).

At lower temperatures (600–800 °C) and high  $p\text{O}_2$ , the slope increases toward 1/4 to 1/5 with decreasing temperature. This is indicative of extrinsic V<sup>••</sup><sub>O</sub> contribution. In this case, the conditions  $\sigma_{\text{Ge}} \gg \sigma_{\text{GV}_\text{O}}$  and [V<sup>••</sup><sub>O</sub>]<sub>ext</sub>  $\gg$  [V<sup>••</sup><sub>O</sub>]<sub>int</sub> apply. The conductivity is dominantly electronic, but the denominator  $n$  changes from 6 to 4 [18]. If  $\sigma_{\text{Ge}} \ll \sigma_{\text{GV}_\text{O}}$  and [V<sup>••</sup><sub>O</sub>]<sub>int</sub> < [V<sup>••</sup><sub>O</sub>]<sub>ext</sub> apply, the electrical conductivity is dominated by ionic transport via extrinsic V<sup>••</sup><sub>O</sub>, showing (in the extreme case of pure ionic transport) no dependence on  $p\text{O}_2$ . The intermediate case, as observed here at 600–800 °C, is characterized by  $4 < n < 6$ , where  $n$  increases with temperature [18]. In the high  $p\text{O}_2$  regime, this would correspond to an increase of [V<sup>••</sup><sub>O</sub>]<sub>int</sub>, whereas at low  $p\text{O}_2$ —to a dissociation of dimer or trimer defect complexes.

The very high values of  $n$ , observed in Ce<sub>0.33</sub>–Zr<sub>0.67</sub>O<sub>2-δ</sub> at 600–800 °C for high  $p\text{O}_2$ , apparently correspond to the case of  $\sigma_{\text{Ge}} \approx \sigma_{\text{GV}_\text{O}}$ , where  $\sigma_{\text{GV}_\text{O}}$  is defined by the very high and constant [V<sup>••</sup><sub>O</sub>]<sub>ext</sub>, leading to an almost  $p\text{O}_2$ -independent conductivity at

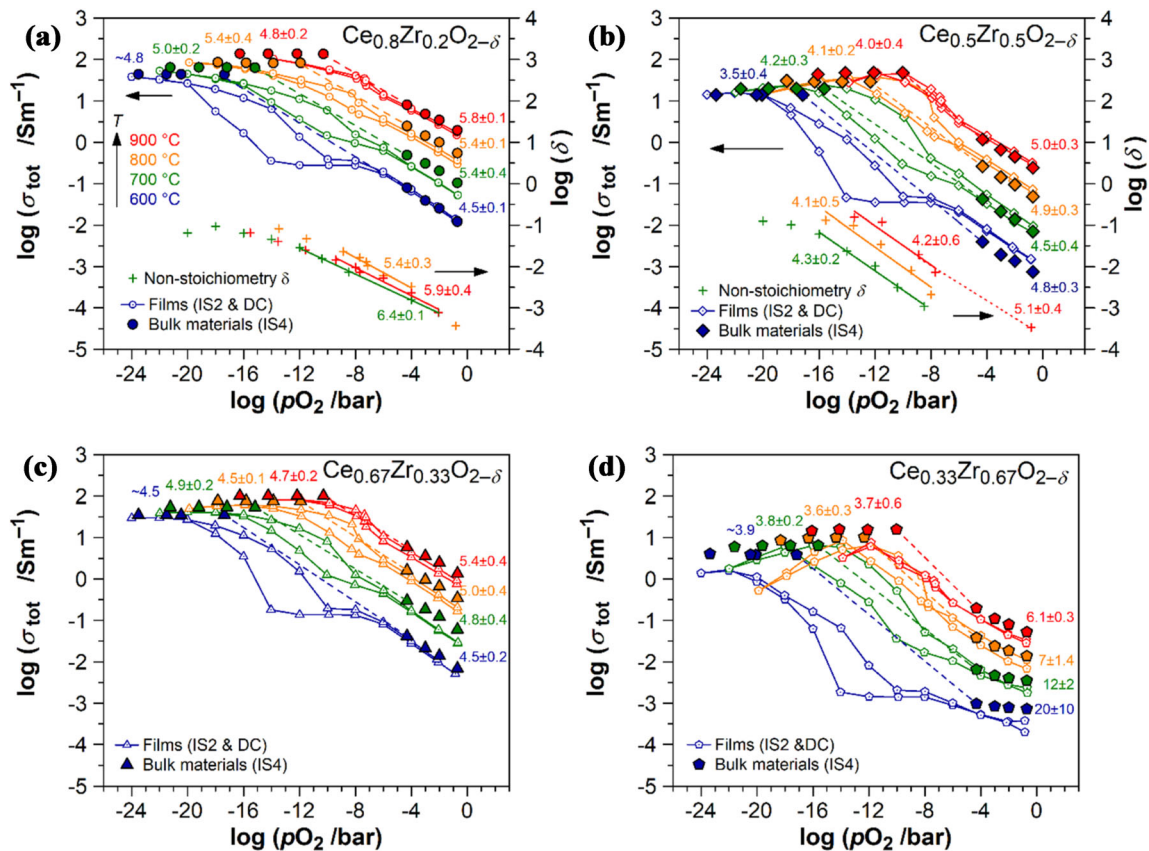


**Figure 7** Electrical conductivity  $\sigma_{\text{tot}}$  of  $\text{Ce}_{1-x}\text{Zr}_x\text{O}_{2-\delta}$  under reducing atmospheres. The correlation with non-stoichiometry data from [29] is shown for  $\text{Ce}_{0.8}\text{Zr}_{0.2}\text{O}_{2-\delta}$  and  $\text{Ce}_{0.5}\text{Zr}_{0.5}\text{O}_{2-\delta}$ . The

600 °C. Apparently, the same situation occurs in  $\text{CeO}_{2-\delta}$  films, with the exception that pure ceria in this study contained much less impurities than CZO [29]. While at 800–900 °C the conductivity of bulk  $\text{CeO}_{2-\delta}$  follows the classic  $p\text{O}_2$ -dependence, at 600–700 °C the total conductivity  $\sigma_{\text{tot}}$  is less dependent on  $p\text{O}_2$  in oxidizing conditions (Fig. 8b). The  $\sigma_{\text{G}}$  at 600 °C is nearly independent on  $p\text{O}_2$ , suggesting the conductivity via extrinsic  $\text{V}_\text{O}^{\bullet\bullet}$ . Consistent with insights from  $\sigma_{\text{tot}}(T)$  dependences in Fig. 6b, at 700 °C the  $\sigma_{\text{G}}$  of bulk  $\text{CeO}_{2-\delta}$  shows a purely electronic nature with a conventional  $(p\text{O}_2)^{-1/6}$  dependence. These two observations of  $\sigma_{\text{G}}$  support the earlier made assignment of dominantly electronic conductivity with the high-temperature ( $T > 680$  °C) regime and of dominated by impurity-related extrinsic charge carriers transport with the low-temperature one (Fig. 6b) for bulk  $\text{CeO}_{2-\delta}$ . On the contrary, for  $\text{CeO}_{2-\delta}$  films,  $n$  increases with temperature at high  $p\text{O}_2$  and decreases toward 6 (slope  $-1/6$ ) at the lowest

numbers next to the curves indicate the slope, i.e., the denominator  $n$  in the  $\sigma$  vs  $(p\text{O}_2)^{-1/n}$  representation. The origin of hysteresis in film conductivities at moderate  $p\text{O}_2$  is described in [29].

oxygen activities and highest temperatures (Fig. 8a). In light of usually higher ionic contribution in  $\sigma_{\text{tot}}$  of nanostructured CZO [26], we assume that the observed discrepancies between bulk and PLD film ceria may be related to the smaller grain size of  $\text{CeO}_{2-\delta}$  films. The overall much higher electrical conductivity of  $\text{CeO}_{2-\delta}$  films compared to their bulk counterparts, both in  $\sigma_{\text{tot}}(T)$  in air and  $\sigma_{\text{tot}}(p\text{O}_2)$  measurements, supports this assumption. Note that for another “more ionic” film material, the  $\text{Ce}_{0.33}\text{Zr}_{0.67}\text{O}_{2-\delta}$ , an electronic-like increase of  $E_a$  (unlike “the deceleration” of the slope for  $\text{CeO}_{2-\delta}$ ) is seen in Fig. 6a, which supports the afore-mentioned assumption about the dominating influence of Zr addition over that of microstructural peculiarities in Zr-substituted ceria. The as of now available experimental results, however, do not allow us to confirm the effect of microstructure and to derive the related mechanism behind this conductivity behavior of film  $\text{CeO}_{2-\delta}$ .

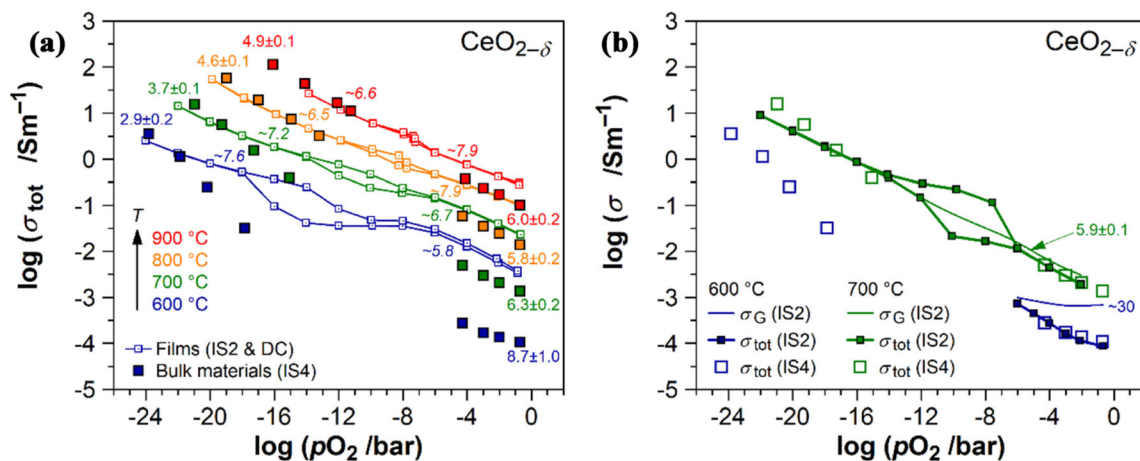


**Figure 8** Electrical conductivity of bulk and film  $\text{CeO}_{2-\delta}$  (a) and its extracted grain interior conductivity  $\sigma_G$  (b) under reducing atmosphere. The numbers next to the curves indicate the slope, i.e.,

the denominator  $n$  in  $\sigma \sim (p\text{O}_2)^{-1/n}$  dependences (italic numbers—for films).

### Conclusion

By applying two- and four-point impedance spectroscopy, the artefactual contributions of electrode polarization effects could be successfully separated from the conductivity data for bulk and PLD film  $\text{Ce}_{1-x}\text{Zr}_x\text{O}_{2-\delta}$ . It was established that in the temperature range that are typical operating conditions of automotive TWC, the CZO conductivity is dominantly electronic and is determined by the grain conductivity, whereas other possible contributions in conductivity are negligible in the temperature range of 700–900 °C. The structural peculiarities, potentially, play a significant role in the conductivity of pure nano-grained ceria films, rendering this material to behave more “ionic-like”. The substitution of Zr for Ce in CZO, apparently, does not support these contributions. The beneficial effect of Zr addition appears to dominate any possible microstructural effects on the conductivity of CZO films and drives these materials to a strongly electronic conductivity at temperatures even 200 K lower than those observed for mixed ionic/electronic to electronic conductivity transitions in bulk or film  $\text{CeO}_2$ . Consequently, the film and bulk  $\text{Ce}_{1-x}\text{Zr}_x\text{O}_{2-\delta}$  show qualitatively similar electrochemical behavior in reducing conditions, which could be adequately described in the framework of conventional defect model for ceria derivatives without the introduction of possible microstructural impacts.

### Acknowledgements

The authors are indebted to Ms. S. Lenk for the acquisition of the SEM images and elemental analysis by EDS, to W. Dziony for high-resolution SEM characterization, and to K. Meyer for the XRD measurements (all from Clausthal University of Technology). This research was funded by the German Research Foundation (Deutsche Forschungsgemeinschaft, DFG), Grants FR 1301/23-1 and MO 1060/29-1.

### Author contributions

I.K., C.S., A.W., G.H., R.M., and H.F. conceived and designed the methodology; C.S. synthesized the starting materials, fabricated the bulk CZO specimens and PLD targets, performed their XRD characterization, and measured their electrical conductivity with IS4; I.K. and A.W. prepared the film CZO specimens, performed the IS2 and DC measurements of electrical conductivity of bulk and film CZO and analyzed the data; H.W. performed the XRD characterization of film samples. All together evaluated and discussed the results and wrote the paper.

### Funding

Open Access funding enabled and organized by Projekt DEAL.

## Data availability

All relevant data presented in the article are stored according to institutional requirements and as such are not available online. However, all data used in this manuscript can be made available upon request to the authors.

## Declarations

**Conflict of interest** The authors declare no conflicts of interests.

**Open Access** This article is licensed under a Creative Commons Attribution 4.0 International License, which permits use, sharing, adaptation, distribution and reproduction in any medium or format, as long as you give appropriate credit to the original author(s) and the source, provide a link to the Creative Commons licence, and indicate if changes were made. The images or other third party material in this article are included in the article's Creative Commons licence, unless indicated otherwise in a credit line to the material. If material is not included in the article's Creative Commons licence and your intended use is not permitted by statutory regulation or exceeds the permitted use, you will need to obtain permission directly from the copyright holder. To view a copy of this licence, visit <http://creativecommons.org/licenses/by/4.0/>.

## References

- [1] Trovarelli A (1996) Catalytic properties of ceria and CeO<sub>2</sub>-containing materials. *Catal Rev Sci Eng* 38:439–520. <https://doi.org/10.1080/01614949608006464>
- [2] Di Monte R, Kašpar J (2004) On the role of oxygen storage in three-way catalysis. *Top Catal* 28:47–57. <https://doi.org/10.1023/B:TOCA.0000024333.08447.f7>
- [3] Lott P, Deutschmann O (2021) Lean-burn natural gas engines: challenges and concepts for an efficient exhaust gas aftertreatment system. *Emiss Control Sci Technol* 7:1–6. <https://doi.org/10.1007/s40825-020-00176-w>
- [4] Rood S, Eslava S, Manigrasso A, Bannister C (2020) Recent advances in gasoline three-way catalyst formulation: a review. *Proc Inst Mech Eng, Part D J Automobile Eng* 234:936–949. <https://doi.org/10.1177/0954407019859822>
- [5] Sugiura M, Ozawa M, Suda A, Suzuki T, Kanazawa T (2005) Development of innovative three-way catalysts containing ceria-zirconia solid solutions with high oxygen storage/release capacity. *Bull Chem Soc Jpn* 78:752–767. <https://doi.org/10.1246/bcsj.78.752>
- [6] Moos R (2010) Catalysts as sensors—A promising novel approach in automotive exhaust gas aftertreatment. *Sensors* 10:6773–6787. <https://doi.org/10.3390/s100706773>
- [7] Kuhn M, Bishop SR, Rupp JLM, Tuller HL (2013) Structural characterization and oxygen nonstoichiometry of ceria-zirconia (Ce<sub>1-x</sub>Zr<sub>x</sub>O<sub>2-δ</sub>) solid solutions. *Acta Mater* 61:4277–4288. <https://doi.org/10.1016/j.actamat.2013.04.001>
- [8] Devaiah D, Reddy LH, Park S-E, Reddy BM (2018) Ceria-zirconia mixed oxides: synthetic methods and applications. *Catal Rev* 60:177–277. <https://doi.org/10.1080/01614940.2017.1415058>
- [9] Aneggi E, Boaro M, Colussi S, De Leitenburg C, Trovarelli A (2016) Ceria-based materials in catalysis: historical perspective and future trends. In: Bünzli J-CG, Pecharsky VK (eds) *Handbook on the physics and chemistry of rare earths*. Elsevier, Netherlands
- [10] Andriopoulou C, Harris D, Stephenson H, Efstathiou AM, Boghosian S (2020) In situ Raman spectroscopy as a tool for discerning subtle structural differences between commercial (Ce, Zr)O<sub>2</sub>-based OSC materials of identical composition. *Catalysts* 10:462. <https://doi.org/10.3390/catal10040462>
- [11] Chen D, Cao Y, Weng D, Tuller HL (2014) Defect and transport model of ceria-zirconia solid solutions: Ce<sub>0.8</sub>Zr<sub>0.2</sub>O<sub>2-δ</sub>—An electrical conductivity study. *Chem Mater* 26:5143–5150. <https://doi.org/10.1021/cm502565b>
- [12] Chiodelli G, Flora G, Scagliotti M (1996) Electrical properties of the ZrO<sub>2</sub>–CeO<sub>2</sub> system. *Solid State Ionics* 91:109–121. [https://doi.org/10.1016/S0167-2738\(96\)00382-7](https://doi.org/10.1016/S0167-2738(96)00382-7)
- [13] Yang Z, Woo TK, Hermansson K (2006) Effects of Zr doping on stoichiometric and reduced ceria: a first-principles study. *J Chem Phys* 124:224704. <https://doi.org/10.1063/1.2200354>
- [14] Tuller HL, Nowick AS (1979) Defect structure and electrical properties of nonstoichiometric CeO<sub>2</sub> single crystals. *J Electrochem Soc* 126:209–217. <https://doi.org/10.1149/1.2129007>
- [15] Panhans MA, Blumenthal RN (1993) A thermodynamic and electrical conductivity study of nonstoichiometric cerium dioxide. *Solid State Ionics* 60:279–298. [https://doi.org/10.1016/0167-2738\(93\)90006-0](https://doi.org/10.1016/0167-2738(93)90006-0)
- [16] Schmitt R, Nanning A, Kraynys O, Korobko R, Frenkel AI, Lubomirsky I, Haile SM, Rupp JLM (2020) A review of defect structure and chemistry in ceria and its solid solutions. *Chem Soc Rev* 49:554–592. <https://doi.org/10.1039/C9CS00588A>



- [17] Tuller HL, Nowick AS (1977) Small polaron electron transport in reduced CeO<sub>2</sub> single crystals. *J Phys Chem Solids* 38:859–867. [https://doi.org/10.1016/0022-3697\(77\)90124-X](https://doi.org/10.1016/0022-3697(77)90124-X)
- [18] Izu N, Shin W, Matsubara I, Murayama N (2004) Resistive oxygen gas sensors using ceria-zirconia thick films. *J Ceram Soc Jpn* 112:535–539. <https://doi.org/10.14852/jcersjsuppl.112.0.S535.0>
- [19] Izu N, Oh-hori N, Itou M, Shin W, Matsubara I, Murayama N (2005) Resistive oxygen gas sensors based on Ce<sub>1-x</sub>Zr<sub>x</sub>O<sub>2</sub> nano powder prepared using new precipitation method. *Sens Actuat B Chem* 108:238–243. <https://doi.org/10.1016/j.snb.2004.11.064>
- [20] Izu N, Oh-hori N, Shin W, Matsubara I, Murayama N, Itou M (2008) Response of resistive oxygen sensors using Ce<sub>1-x</sub>Zr<sub>x</sub>O<sub>2</sub> (x = 0.05, 0.10) thick films in propane combustion gas. *Sens Actuat B Chem* 130:105–109. <https://doi.org/10.1016/j.snb.2007.07.093>
- [21] Melchionna M, Fornasiero P (2014) The role of ceria-based nanostructured materials in energy applications. *Mater Today* 17:349–357. <https://doi.org/10.1016/j.mattod.2014.05.005>
- [22] Hartmann P, Brezesinski T, Sann J, Lotnyk A, Eufinger J-P, Kienle L, Janek J (2013) Defect chemistry of oxide nanomaterials with high surface area: ordered mesoporous thin films of the oxygen storage catalyst CeO<sub>2</sub>-ZrO<sub>2</sub>. *ACS Nano* 7:2999–3013. <https://doi.org/10.1021/nn400255w>
- [23] Göbel MC, Gregori G, Guo X, Maier J (2010) Boundary effects on the electrical conductivity of pure and doped cerium oxide thin films. *Phys Chem Chem Phys* 12:14351–14361. <https://doi.org/10.1039/c0cp00385a>
- [24] Chiang Y-M, Lavik EB, Kosacki I, Tuller HL, Ying JY (1996) Defect and transport properties of nanocrystalline CeO<sub>2-x</sub>. *Appl Phys Lett* 69:185–187. <https://doi.org/10.1063/1.117366>
- [25] Knauth P, Engel J, Bishop SR, Tuller HL (2015) Study of compaction and sintering of nanosized oxide powders by in situ electrical measurements and dilatometry: nano CeO<sub>2</sub>-case study. *J Electroceram* 34:82–90. <https://doi.org/10.1007/s10832-014-9946-9>
- [26] Boaro M, Trovarelli A, Hwang J-H, Mason TO (2002) Electrical and oxygen storage/release properties of nanocrystalline ceria-zirconia solid solutions. *Solid State Ionics* 147:85–95. [https://doi.org/10.1016/S0167-2738\(02\)0004-8](https://doi.org/10.1016/S0167-2738(02)0004-8)
- [27] Kosacki I, Suzuki T, Petrovsky V, Anderson HU (2000) Electrical conductivity of nanocrystalline ceria and zirconia thin films. *Solid State Ionics* 136–137:1225–1233. [https://doi.org/10.1016/S0167-2738\(00\)00591-9](https://doi.org/10.1016/S0167-2738(00)00591-9)
- [28] Zhu B, Luo X, Xia C, Albinsson I, Mellander B-E (1997) Electrical properties of ZrO<sub>2</sub>-CeO<sub>2</sub> at intermediate temperatures. *Ionics* 3:363–367. <https://doi.org/10.1007/BF02375711>
- [29] Kogut I, Wollbrink A, Steiner C, Wulfmeier H, El Azzouzi F-E, Moos R, Fritze H (2021) Linking the electrical conductivity and non-stoichiometry of thin film Ce<sub>1-x</sub>Zr<sub>x</sub>O<sub>2-δ</sub> by a resonant nanobalance approach. *Materials* 14(4):748. <https://doi.org/10.3390/ma14040748>
- [30] Patterson AL (1939) The Scherrer formula for X-Ray particle size determination. *Phys Rev* 56:978–982. <https://doi.org/10.1103/PhysRev.56.978>
- [31] Pecharsky VK, Zavalij PY (2009) Fundamentals of powder diffraction and structural characterization of materials, 2nd edn. Springer, New York
- [32] McCusker LB, Von Dreele RB, Cox DE, Louër D, Scardi P (1999) Rietveld refinement guidelines. *J Appl Cryst* 32:36–50. <https://doi.org/10.1107/S0021889898009856>
- [33] Hagen G, Kita J, Izu N, Röder-Roith U, Schönauer-Kamin D, Moos R (2013) Planar platform for temperature dependent four-wire impedance spectroscopy—A novel tool for the characterization of functional materials. *Sens Actuators B Chem* 187:174–183. <https://doi.org/10.1016/j.snb.2012.10.068>
- [34] Schulz M, Fritze H, Stenzel C (2013) Measurement and control of oxygen partial pressure at elevated temperatures. *Sens Actuators B Chem* 187:503–508. <https://doi.org/10.1016/j.snb.2013.02.115>
- [35] Varez A, Garcia-Gonzalez E, Jolly J, Sanz J (2007) Structural characterization of Ce<sub>1-x</sub>Zr<sub>x</sub>O<sub>2</sub> (0 ≤ x ≤ 1) samples prepared at 1650 °C by solid state reaction. A combined TEM and XRD study. *J Eur Ceram Soc* 27:3677–3682. <https://doi.org/10.1016/j.jeurceramsoc.2007.02.014>
- [36] Meriani S, Spinolo G (1987) Powder data for metastable Zr<sub>x</sub>Ce<sub>1-x</sub>O<sub>2</sub> (x = 0.84 to 0.40) solid solutions with tetragonal symmetry. *Powder Diffr* 2(4):255–256. <https://doi.org/10.1017/S0885715600012914>
- [37] Joo JH, Choi GM (2007) Electrical conductivity of thin film ceria grown by pulsed laser deposition. *J Eur Ceram Soc* 27:4273–4277. <https://doi.org/10.1016/j.jeurceramsoc.2007.02.135>
- [38] Bishop SR, Nakamura T, Amezawa K (2014) Chemically-induced expansion of Zr<sub>0.2</sub>Ce<sub>0.8</sub>O<sub>2-δ</sub>. *Solid State Ionics* 261:1–4. <https://doi.org/10.1016/j.ssi.2014.03.026>
- [39] Koettgen J, Martin M (2020) The ionic conductivity of Sm-doped ceria. *J Am Ceram Soc* 103:3776–3787. <https://doi.org/10.1111/jace.17066>
- [40] Parras JP, Cao C, Ma Z, Mücke R, Jin L, Dunin-Borkowski R, Guillon O, De Souza RA (2019) The grain-boundary resistance of CeO<sub>2</sub> ceramics: a combined microscopy-

- spectroscopy-simulation study of a dilute solution. *J Am Ceram Soc* 103:1755–1764. <https://doi.org/10.1111/jace.16843>
- [41] Souza ECC, Chueh WC, Jung W, Muccillo ENS, Haile SM (2012) Ionic and electronic conductivity of nanostructured Samaria-Doped Ceria. *J Electrochem Soc* 159(5):K127–K135. <https://doi.org/10.1149/2.056205jes>
- [42] Xiong Y-P, Kishimoto H, Yamaji K, Yoshinaga M, Horita T, Brito ME, Yokokawa H (2011) Electronic conductivity of pure ceria. *Solid State Ionics* 192:476–479. <https://doi.org/10.1016/j.ssi.2010.07.017>
- [43] Zhou X-D, Anderson HU, Huebner W (2002) Grain size and chemical composition effects on the grain boundary resistance of ceria. *Mat Res Soc Symp Proc* 730:44. <https://doi.org/10.1557/PROC-730-V4.4>
- [44] Kežionis A, Butvilas P, Šalkus T, Kazlauskas S, Petrušionis D, Žukauskas T, Kazakevičius E, Orliukas AF (2013) Four-electrode impedance spectrometer for investigation of solid ion conductors. *Rev Sci Instrum* 84:013902. <https://doi.org/10.1063/1.4774391>
- [45] Ishaï PB, Talary MS, Caduff A, Levy E, Feldman Y (2013) Electrode polarization in dielectric measurements: a review. *Meas Sci Technol* 24:102001. <https://doi.org/10.1088/0957-0233/24/10/102001>
- [46] Dygas JR, Fafilek G, Breiter MW (1999) Study of grain boundary polarization by two-probe and four-probe impedance spectroscopy. *Solid State Ionics* 119:115–125. [https://doi.org/10.1016/S0167-2738\(98\)00492-5](https://doi.org/10.1016/S0167-2738(98)00492-5)
- [47] Anderson EL, Bühlmann P (2016) Electrochemical impedance spectroscopy of ion-selective membranes: artifacts in two-, three-, and four-electrode measurements. *Anal Chem* 88(19):9738–9745. <https://doi.org/10.1021/acs.analchem.6b02641>
- [48] Lee J-H, Yoon SM, Kim B-K, Lee H-W, Song HS (2002) Electrical conductivity and defect structure of CeO<sub>2</sub>-ZrO<sub>2</sub> mixed oxide. *J Mater Sci* 37:1165–1171. <https://doi.org/10.1023/A:1014363304942>
- [49] Reiß S, Wedemann M, Moos R, Rösch M (2009) Electrical in-situ characterization of three-way catalyst coatings. *Top Catal* 52:1898–1902. <https://doi.org/10.1007/s11244-009-9366-2>
- [50] Beulertz G, Votsmeier M, Moos R (2015) Effect of propene, propane, and methane on conversion and oxidation state of three-way catalysts: a microwave cavity perturbation study. *Appl Catal B-Environ* 165:369–377. <https://doi.org/10.1016/j.apcatb.2014.09.068>
- [51] Steiner C, Walter S, Malashchuk V, Hagen G, Kogut I, Fritze H, Moos R (2020) Determination of the dielectric properties of storage materials for exhaust gas aftertreatment using the microwave cavity perturbation method. *Sensors* 20:6024. <https://doi.org/10.3390/s20216024>
- [52] Reidy RF, Simkovich G (1993) Electrical conductivity and point defect behavior in ceria-stabilized zirconia. *Solid State Ionics* 62:85–97. [https://doi.org/10.1016/0167-2738\(93\)90255-2](https://doi.org/10.1016/0167-2738(93)90255-2)

**Publisher's Note** Springer Nature remains neutral with regard to jurisdictional claims in published maps and institutional affiliations.